

Broadband transparent and CMOS-compatible flat optics with silicon nitride metasurfaces [Invited]

SHANE COLBURN,^{1,*} ALAN ZHAN,² ELYAS BAYATI,¹ JAMES WHITEHEAD,¹
ALBERT RYOU,¹ LUOCHENG HUANG,³ AND ARKA MAJUMDAR^{1,2}

¹Department of Electrical Engineering, University of Washington, Seattle, WA 98195, USA

²Department of Physics, University of Washington, Seattle, WA 98195, USA

³Department of Materials Science and Engineering, University of Washington, Seattle, WA 98195, USA

*scolbur2@uw.edu

Abstract: Metasurface optics is a promising candidate for realizing the next generation of miniaturized optical components. Unlike refractive optics, these devices modify light over a wavelength-scale thickness, changing the phase, amplitude, and polarization. This review details recent developments and state-of-the-art metasurfaces realized using silicon nitride. We emphasize this material as to date it has the lowest refractive index with which metasurfaces have been experimentally demonstrated. The wide band gap of silicon nitride enables reduced absorption over a broad wavelength range relative to its higher index counterparts, providing a CMOS-compatible platform for producing a variety of high efficiency metasurface elements and systems.

© 2018 Optical Society of America under the terms of the [OSA Open Access Publishing Agreement](#)

OCIS codes: (050.6624) Subwavelength structures; (050.1965) Diffractive lenses; (220.4241) Nanostructure fabrication; (160.3918) Metamaterials; (290.4020) Mie theory; (050.1970) Diffractive optics.

References and links

1. N. Yu and F. Capasso, "Flat optics with designer metasurfaces," *Nat. Mater.* **13**(2), 139–150 (2014).
2. A. V. Kildishev, A. Boltasseva, and V. M. Shalaev, "Planar photonics with metasurfaces," *Science* **339**(6125), 1232009 (2013).
3. N. Yu, P. Genevet, M. A. Kats, F. Aieta, J.-P. Tetienne, F. Capasso, and Z. Gaburro, "Light propagation with phase discontinuities: generalized laws of reflection and refraction," *Science* **334**(6054), 333–337 (2011).
4. D. Fattal, J. Li, Z. Peng, M. Fiorentino, and R. G. Beausoleil, "Flat dielectric grating reflectors with focusing abilities," *Nat. Photonics* **4**(7), 466–470 (2010).
5. D. Lin, M. Melli, E. Poliakov, P. S. Hilaire, S. Dhuey, C. Peroz, S. Cabrini, M. Brongersma, and M. Klug, "Optical metasurfaces for high angle steering at visible wavelengths," *Sci. Rep.* **7**(1), 2286 (2017).
6. D. Fattal, Z. Peng, T. Tran, S. Vo, M. Fiorentino, J. Brug, and R. G. Beausoleil, "A multi-directional backlight for a wide-angle, glasses-free three-dimensional display," *Nature* **495**(7441), 348–351 (2013).
7. X. Ni, S. Ishii, A. V. Kildishev, and V. M. Shalaev, "Ultra-thin, planar, Babinet-inverted plasmonic metalenses," *Light Sci. Appl.* **2**(4), e72 (2013).
8. Y. F. Yu, A. Y. Zhu, R. Paniagua-Domínguez, Y. H. Fu, B. Luk'yanchuk, and A. I. Kuznetsov, "High-transmission dielectric metasurface with 2π phase control at visible wavelengths," *Laser Photonics Rev.* **9**(4), 412–418 (2015).
9. D. Lin, P. Fan, E. Hasman, and M. L. Brongersma, "Dielectric gradient metasurface optical elements," *Science* **345**(6194), 298–302 (2014).
10. A. Arbabi, Y. Horie, A. J. Ball, M. Bagheri, and A. Faraon, "Subwavelength-thick lenses with high numerical apertures and large efficiency based on high-contrast transmitarrays," *Nat. Commun.* **6**, ncomms8069 (2015).
11. K. E. Chong, I. Staude, A. James, J. Dominguez, S. Liu, S. Campione, G. S. Subramania, T. S. Luk, M. Decker, D. N. Neshev, I. Brener, and Y. S. Kivshar, "Polarization-Independent Silicon Metadevices for Efficient Optical Wavefront Control," *Nano Lett.* **15**(8), 5369–5374 (2015).
12. C. Wu, N. Arju, G. Kelp, J. A. Fan, J. Dominguez, E. Gonzales, E. Tutuc, I. Brener, and G. Shvets, "Spectrally selective chiral silicon metasurfaces based on infrared Fano resonances," *Nat. Commun.* **5**(1), 3892 (2014).
13. S. Astilean, P. Lalanne, P. Chavel, E. Cambriil, and H. Launois, "High-efficiency subwavelength diffractive element patterned in a high-refractive-index material for 633 nm," *Opt. Lett.* **23**(7), 552–554 (1998).
14. P. Lalanne, S. Astilean, P. Chavel, E. Cambriil, and H. Launois, "Design and fabrication of blazed binary diffractive elements with sampling periods smaller than the structural cutoff," *JOSA A* **16**(5), 1143–1156 (1999).

15. M. Khorasaninejad, W. T. Chen, R. C. Devlin, J. Oh, A. Y. Zhu, and F. Capasso, "Metalenses at visible wavelengths: Diffraction-limited focusing and subwavelength resolution imaging," *Science* **352**(6290), 1190–1194 (2016).
16. M. Khorasaninejad, A. Y. Zhu, C. Roques-Carmes, W. T. Chen, J. Oh, I. Mishra, R. C. Devlin, and F. Capasso, "Polarization-Insensitive Metalenses at Visible Wavelengths," *Nano Lett.* **16**(11), 7229–7234 (2016).
17. M. Khorasaninejad, Z. Shi, A. Y. Zhu, W. T. Chen, V. Sanjeev, A. Zaidi, and F. Capasso, "Achromatic Metalens over 60 nm Bandwidth in the Visible and Metalens with Reverse Chromatic Dispersion," *Nano Lett.* **17**(3), 1819–1824 (2017).
18. W. T. Chen, A. Y. Zhu, V. Sanjeev, M. Khorasaninejad, Z. Shi, E. Lee, and F. Capasso, "A broadband achromatic metalens for focusing and imaging in the visible," *Nat. Nanotechnol.* **13**(3), 220–226 (2018).
19. B. H. Chen, P. C. Wu, V.-C. Su, Y.-C. Lai, C. H. Chu, I. C. Lee, J.-W. Chen, Y. H. Chen, Y.-C. Lan, C.-H. Kuan, and D. P. Tsai, "GaN Metalens for Pixel-Level Full-Color Routing at Visible Light," *Nano Lett.* **17**(10), 6345–6352 (2017).
20. S. Wang, P. C. Wu, V.-C. Su, Y.-C. Lai, M.-K. Chen, H. Y. Kuo, B. H. Chen, Y. H. Chen, T.-T. Huang, J.-H. Wang, R.-M. Lin, C.-H. Kuan, T. Li, Z. Wang, S. Zhu, and D. P. Tsai, "A broadband achromatic metalens in the visible," *Nat. Nanotechnol.* **13**(3), 227–232 (2018).
21. A. Zhan, S. Colburn, R. Trivedi, T. K. Fryett, C. M. Dodson, and A. Majumdar, "Low-Contrast Dielectric Metasurface Optics," *ACS Photonics* **3**(2), 209–214 (2016).
22. A. Zhan, S. Colburn, C. M. Dodson, and A. Majumdar, "Metasurface Freeform Nanophotonics," *Sci. Rep.* **7**(1), 1673 (2017).
23. Z.-B. Fan, Z.-K. Shao, M.-Y. Xie, X.-N. Pang, W.-S. Ruan, F.-L. Zhao, Y.-J. Chen, S.-Y. Yu, and J.-W. Dong, "Silicon nitride metalenses for unpolarized high-NA visible imaging," *ArXiv170900573 Phys.* (2017).
24. C. Hong, S. Colburn, and A. Majumdar, "Flat metaform near-eye visor," *Appl. Opt.* **56**(31), 8822–8827 (2017).
25. J. Flannery, R. Al Maruf, T. Yoon, and M. Bajcsy, "Fabry-Pérot Cavity Formed with Dielectric Metasurfaces in a Hollow-Core Fiber," *ACS Photonics* **5**(2), 337–341 (2018).
26. S. Colburn, A. Zhan, and A. Majumdar, "Metasurface optics for full-color computational imaging," *Sci. Adv.* **4**, eaar 2114 (2018).
27. L. Huang, X. Chen, H. Mühlenbernd, H. Zhang, S. Chen, B. Bai, Q. Tan, G. Jin, K. W. Cheah, C. W. Qiu, J. Li, T. Zentgraf, and S. Zhang, "Three-dimensional optical holography using a plasmonic metasurface," *Nat. Commun.* **4**(1), 2808 (2013).
28. E. Karimi, S. A. Schulz, I. De Leon, H. Qassim, J. Upham, and R. W. Boyd, "Generating optical orbital angular momentum at visible wavelengths using a plasmonic metasurface," *Light Sci. Appl.* **3**(5), e167 (2014).
29. F. Ding, Z. Wang, S. He, V. M. Shalaev, and A. V. Kildishev, "Broadband high-efficiency half-wave plate: a supercell-based plasmonic metasurface approach," *ACS Nano* **9**(4), 4111–4119 (2015).
30. Z. H. Jiang, L. Lin, D. Ma, S. Yun, D. H. Werner, Z. Liu, and T. S. Mayer, "Broadband and wide field-of-view plasmonic metasurface-enabled waveplates," *Sci. Rep.* **4**(1), 7511 (2015).
31. R. R. Reddy and Y. Nazeer Ahammed, "A study on the Moss relation," *Infrared Phys. Technol.* **36**(5), 825–830 (1995).
32. Y.-W. Huang, H. W. H. Lee, R. Sokhoyan, R. A. Pala, K. Thyagarajan, S. Han, D. P. Tsai, and H. A. Atwater, "Gate-Tunable Conducting Oxide Metasurfaces," *Nano Lett.* **16**(9), 5319–5325 (2016).
33. J. K. S. Poon and W. D. Sacher, "Multilayer silicon nitride-on-silicon photonic platforms for three-dimensional integrated photonic devices and circuits," in *2017 75th Annual Device Research Conference (DRC)* (2017), pp. 1–2.
34. J. Yang and J. A. Fan, "Analysis of material selection on dielectric metasurface performance," *Opt. Express* **25**(20), 23899–23909 (2017).
35. E. Bayati, A. Zhan, S. Colburn, and A. Majumdar, "The role of refractive index in metalens performance," *ArXiv180504659 Phys.* (2018).
36. Z. Bomzon, G. Biener, V. Kleiner, and E. Hasman, "Radially and azimuthally polarized beams generated by space-variant dielectric subwavelength gratings," *Opt. Lett.* **27**(5), 285–287 (2002).
37. A. Niv, G. Biener, V. Kleiner, and E. Hasman, "Propagation-invariant vectorial Bessel beams obtained by use of quantized Pancharatnam-Berry phase optical elements," *Opt. Lett.* **29**(3), 238–240 (2004).
38. C. J. Chang-Hasnain and W. Yang, "High-contrast gratings for integrated optoelectronics," *Adv. Opt. Photonics* **4**(3), 379–440 (2012).
39. A. Arbabi, R. M. Briggs, Y. Horie, M. Bagheri, and A. Faraon, "Efficient dielectric metasurface collimating lenses for mid-infrared quantum cascade lasers," *Opt. Express* **23**(26), 33310–33317 (2015).
40. P. R. West, J. L. Stewart, A. V. Kildishev, V. M. Shalaev, V. V. Shkunov, F. Strohkendl, Y. A. Zakharenkov, R. K. Dodds, and R. Byren, "All-dielectric subwavelength metasurface focusing lens," *Opt. Express* **22**(21), 26212–26221 (2014).
41. F. Lu, F. G. Sedgwick, V. Karagodsky, C. Chase, and C. J. Chang-Hasnain, "Planar high-numerical-aperture low-loss focusing reflectors and lenses using subwavelength high contrast gratings," *Opt. Express* **18**(12), 12606–12614 (2010).
42. F. Aieta, P. Genevet, M. A. Kats, N. Yu, R. Blanchard, Z. Gaburro, and F. Capasso, "Aberration-free ultrathin flat lenses and axicons at telecom wavelengths based on plasmonic metasurfaces," *Nano Lett.* **12**(9), 4932–4936 (2012).

43. X. Ni, A. V. Kildishev, and V. M. Shalaev, "Metasurface holograms for visible light," *Nat. Commun. Lond.* **4**(1), 2807 (2013).
44. G. Zheng, H. Mühlenerbernd, M. Kenney, G. Li, T. Zentgraf, and S. Zhang, "Metasurface holograms reaching 80% efficiency," *Nat. Nanotechnol.* **10**(4), 308–312 (2015).
45. N. Yu, F. Aieta, P. Genevet, M. A. Kats, Z. Gaburro, and F. Capasso, "A broadband, background-free quarter-wave plate based on plasmonic metasurfaces," *Nano Lett.* **12**(12), 6328–6333 (2012).
46. A. Arbabi, Y. Horie, M. Bagheri, and A. Faraon, "Dielectric metasurfaces for complete control of phase and polarization with subwavelength spatial resolution and high transmission," *Nat. Nanotechnol.* **10**(11), 937–943 (2015).
47. M. I. Shalaev, J. Sun, A. Tsukernik, A. Pandey, K. Nikolskiy, and N. M. Litchinitser, "High-Efficiency All-Dielectric Metasurfaces for Ultracompact Beam Manipulation in Transmission Mode," *Nano Lett.* **15**(9), 6261–6266 (2015).
48. G. Li, M. Kang, S. Chen, S. Zhang, E. Y.-B. Pun, K. W. Cheah, and J. Li, "Spin-Enabled Plasmonic Metasurfaces for Manipulating Orbital Angular Momentum of Light," *Nano Lett.* **13**(9), 4148–4151 (2013).
49. S. Vo, D. Fattal, W. V. Sorin, Z. Peng, T. Tran, M. Fiorentino, and R. G. Beausoleil, "Sub-Wavelength Grating Lenses With a Twist," *IEEE Photonics Technol. Lett.* **26**(13), 1375–1378 (2014).
50. Y. Yang, W. Wang, P. Moitra, I. I. Kravchenko, D. P. Briggs, and J. Valentine, "Dielectric Meta-Reflectarray for Broadband Linear Polarization Conversion and Optical Vortex Generation," *Nano Lett.* **14**(3), 1394–1399 (2014).
51. V. Liu and S. Fan, "S4 : A free electromagnetic solver for layered periodic structures," *Comput. Phys. Commun.* **183**(10), 2233–2244 (2012).
52. J. W. Goodman, *Introduction to Fourier Optics* (Roberts and Company Publishers, 2005).
53. Z. Lin, B. Groever, F. Capasso, A. W. Rodriguez, and M. Lončar, "Topology-Optimized Multilayered Metaoptics," *Phys. Rev. Appl.* **9**(4), 044030 (2018).
54. A. Zhan, T. K. Fryett, S. Colburn, and A. Majumdar, "Inverse design of optical elements based on arrays of dielectric spheres," *Appl. Opt.* **57**(6), 1437–1446 (2018).
55. D. W. Mackowski and M. I. Mishchenko, "Calculation of the T matrix and the scattering matrix for ensembles of spheres," *JOSA A* **13**(11), 2266–2278 (1996).
56. Y. L. Xu, "Electromagnetic scattering by an aggregate of spheres," *Appl. Opt.* **34**(21), 4573–4588 (1995).
57. A. Egel, L. Pattelli, G. Mazzamuto, D. S. Wiersma, and U. Lemmer, "CELES: CUDA-accelerated simulation of electromagnetic scattering by large ensembles of spheres," *J. Quant. Spectrosc. Radiat. Transf.* **199**, 103–110 (2017).
58. S. Colburn, A. Zhan, and A. Majumdar, "Varifocal zoom imaging with large area focal length adjustable metalenses," *ArXiv180507832 Phys.* (2018).
59. A. Arbabi, E. Arbabi, S. M. Kamali, Y. Horie, S. Han, and A. Faraon, "Miniature optical planar camera based on a wide-angle metasurface doublet corrected for monochromatic aberrations," *Nat. Commun.* **7**, ncomms13682 (2016).
60. M. Jang, Y. Horie, A. Shibukawa, J. Brake, Y. Liu, S. M. Kamali, A. Arbabi, H. Ruan, A. Faraon, and C. Yang, "Wavefront shaping with disorder-engineered metasurfaces," *Nat. Photonics* **12**(2), 84–90 (2018).
61. J. R. Leger, D. Chen, and Z. Wang, "Diffractive optical element for mode shaping of a Nd:YAG laser," *Opt. Lett.* **19**(2), 108–110 (1994).
62. F. Heide, M. Rouf, M. B. Hullin, B. Labitzke, W. Heidrich, and A. Kolb, "High-quality Computational Imaging Through Simple Lenses," *ACM Trans Graph* **32**, 149:1–149:14 (2013).
63. F. Heide, M. Steinberger, Y.-T. Tsai, M. Rouf, D. Pajak, D. Reddy, O. Gallo, J. Liu, W. Heidrich, K. Egiazarian, J. Kautz, and K. Pulli, "FlexISP: A Flexible Camera Image Processing Framework," *ACM Trans Graph* **33**, 231:1–231:13 (2014).
64. W. T. Cathey and E. R. Dowski, "New paradigm for imaging systems," *Appl. Opt.* **41**(29), 6080–6092 (2002).
65. H. B. Wach, E. R. Dowski, Jr., and W. T. Cathey, "Control of chromatic focal shift through wave-front coding," *Appl. Opt.* **37**(23), 5359–5367 (1998).
66. I. M. Vellekoop, A. Lagendijk, and A. P. Mosk, "Exploiting disorder for perfect focusing," *Nat. Photonics* **4**(5), 320–322 (2010).
67. I. M. Vellekoop and C. M. Aegerter, "Scattered light fluorescence microscopy: imaging through turbid layers," *Opt. Lett.* **35**(8), 1245–1247 (2010).
68. E. G. van Putten, D. Akbulut, J. Bertolotti, W. L. Vos, A. Lagendijk, and A. P. Mosk, "Scattering lens resolves sub-100 nm structures with visible light," *Phys. Rev. Lett.* **106**(19), 193905 (2011).
69. J. H. Park, C. Park, H. Yu, J. Park, S. Han, J. Shin, S. H. Ko, K. T. Nam, Y. H. Cho, and Y. Park, "Subwavelength light focusing using random nanoparticles," *Nat. Photonics* **7**(6), 454–458 (2013).
70. J. Ryu, M. Jang, T. J. Eom, C. Yang, and E. Chung, "Optical phase conjugation assisted scattering lens: variable focusing and 3D patterning," *Sci. Rep.* **6**(1), 23494 (2016).
71. A. Boniface, M. Mounaix, B. Blochet, R. Piestun, and S. Gigan, "Transmission-matrix-based point-spread-function engineering through a complex medium," *Optica* **4**(1), 54–59 (2017).
72. H. Yu, K. Lee, J. Park, and Y. Park, "Ultrahigh-definition dynamic 3D holographic display by active control of volume speckle fields," *Nat. Photonics* **11**(3), 186–192 (2017).
73. D. D. Battista, D. Ancora, H. Zhang, K. Lemonaki, E. Marakis, E. Liapis, S. Tzortzakis, and G. Zacharakis, "Tailored light sheets through opaque cylindrical lenses," *Optica* **3**(11), 1237–1240 (2016).

74. Y. Choi, T. D. Yang, C. Fang-Yen, P. Kang, K. J. Lee, R. R. Dasari, M. S. Feld, and W. Choi, "Overcoming the Diffraction Limit Using Multiple Light Scattering in a Highly Disordered Medium," *Phys. Rev. Lett.* **107**(2), 023902 (2011).
75. S. M. Popoff, G. Lerosey, M. Fink, A. C. Boccara, and S. Gigan, "Controlling light through optical disordered media: transmission matrix approach," *New J. Phys.* **13**(12), 123021 (2011).
76. M. Kim, W. Choi, Y. Choi, C. Yoon, and W. Choi, "Transmission matrix of a scattering medium and its applications in biophotonics," *Opt. Express* **23**(10), 12648–12668 (2015).
77. S. M. Popoff, G. Lerosey, R. Carminati, M. Fink, A. C. Boccara, and S. Gigan, "Measuring the transmission matrix in optics: an approach to the study and control of light propagation in disordered media," *Phys. Rev. Lett.* **104**(10), 100601 (2010).
78. T. D. Gerke and R. Piestun, "Aperiodic volume optics," *Nat. Photonics* **4**(3), 188–193 (2010).
79. A. D. Dupuy, Y. Koder, and J. E. Garay, "Unprecedented Electro-Optic Performance in Lead-Free Transparent Ceramics," *Adv. Mater.* **28**(36), 7970–7977 (2016).

1. Introduction

Metasurfaces have generated substantial research interest and attention in recent years. These ultrathin elements comprising arrays of subwavelength-spaced scattering elements can achieve a broad class of functionalities in a flat form factor, transforming the phase, amplitude, and polarization of incident electromagnetic radiation [1–3]. At optical frequencies, the promise of creating miniaturized imaging systems and multiplexing several functionalities into a single device has driven research in both academic and industrial labs [4–6]. While much of the initial research investigated silicon and metal-based metasurfaces [1,4,7–12] for use in transformation optics and integrated optics, lower index materials became appealing because of their transparency at visible wavelengths where there are numerous applications in imaging, display, and spectroscopy. This initiated an exploration into low-loss dielectric platforms that could support high efficiency operation at visible wavelengths, producing a wide array of flat and visible wavelength metasurface elements and optical systems [13–26]. In this review, we begin in Section 2 by conducting a survey of existing low-loss materials employed in metasurface design, expanding on advantages and disadvantages of the material platforms. As silicon nitride (SiN) is the widest band gap and lowest refractive index material experimentally demonstrated as a metasurface scatterer to date [21], we primarily focus on this material in the succeeding sections. We expand on design methodologies in Section 3, detail state-of-the-art SiN metasurface elements and systems in Sections 4 and 5, discuss future directions in Section 6, and conclude in Section 7.

2. Materials survey

Many of the earlier works on optical metasurfaces were based on metallic scatterers [7,27–30]. The high plasma frequency of metals prevented these devices from working in transmission mode and the losses limited efficiency even for reflective devices. Silicon-based metasurfaces [4,8–12] enabled much lower loss devices that could operate efficiently both in reflection and transmission at infrared wavelengths. Recently, however, a wide range of lower refractive index materials have gained popularity as choices for scattering elements in optical metasurfaces due to their reduced optical absorption at visible wavelengths. Semiconductors generally obey the empirical Moss relation [31], where $n^4 \sim 1/E_{gap}$, motivating the selection of lower refractive index materials to increase the band gap and limit absorption. Such materials include titanium dioxide [13–18], gallium nitride [19,20], indium tin oxide [32], and silicon nitride [21–23].

Titanium dioxide has gained popularity as a metasurface material [Fig. 1 (a)-(b)] because of its relatively high index ($n \sim 2.6$) while being transparent across the visible regime. While this material was previously used a couple decades back to make subwavelength blazed gratings [13,14], the platform was only recently popularized for metasurfaces after it enabled the first demonstration of imaging at visible wavelengths using a metasurface [15]. It has since allowed for a variety of metasurfaces [16,17], including a lens designed to be achromatic across the whole visible spectrum [18]. While the optical properties of titanium

dioxide make it a great choice for metasurface scatterers as its absorption is low, yet the refractive index is high enough to provide strong optical confinement, from a practical viewpoint this material has several limitations. These limitations primarily arise from scalable manufacturing concerns as titanium dioxide is deposited slowly via atomic layer deposition, limiting manufacturing throughput. As such, the material cannot leverage current CMOS-compatible foundry infrastructure for mass production, potentially hindering widespread adoption of the platform.

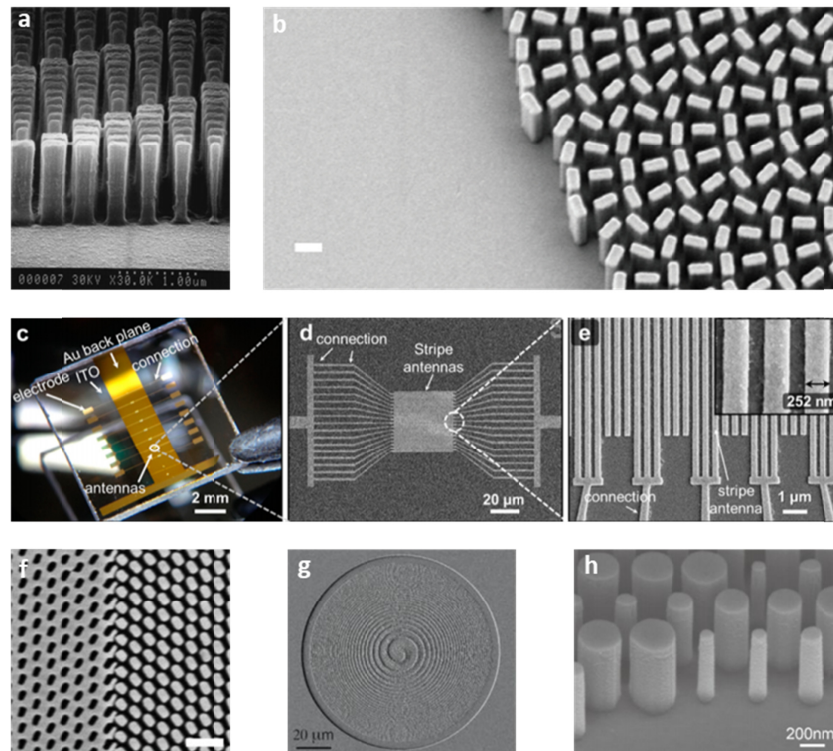


Fig. 1. Existing metasurface platforms employing materials with refractive indices less than that of silicon. Titanium oxide nanopillars [14] (a) and nanofins [15] (b) used for visible wavelength metasurfaces. Scale bar, 300 nm in (b). (c)-(e) Au-based 1D phase gratings with electrical control using index modulation of ITO for tunable beam deflection [32]. Adapted with permission from [32]. Copyright (2016) American Chemical Society. (f) Gallium nitride-based scatterers used in a broadband achromatic lens design with a scale bar of 10 μm [20]. SiN nanoposts used in a vortex beam [21] (g) and as part of a lens [23] (h).

Gallium nitride ($n \sim 2.4$) has also found use in scatterer design in visible wavelength metasurfaces. It shares the relatively high refractive index and visible frequency transparency found in titanium dioxide. A metasurface full-color router for a Bayer pattern pixel used gallium nitride nanoposts [19] to discriminate red, green, and blue wavelengths and focus them to different positions. Separately, a gallium nitride-based achromatic lens was recently realized [20] [Fig. 1 (f)], providing broadband imaging at visible frequencies. While this material is promising in terms of optical properties, gallium nitride would also be difficult to adopt in existing CMOS foundries, like titanium dioxide.

Another existing material with index less than that of silicon used for metasurfaces is indium tin oxide (ITO) ($n \sim 2$). This material is not only transparent at visible wavelengths but is also conductive. The conductive properties of ITO are already being exploited to realize reconfigurable metasurfaces, using field-effect modulation of the refractive index to control the modes and resonances within adjacent scatterers. This index modulation enabled dynamic

beam deflection by applying a spatially varying voltage to a gold grating with the change in the ITO's refractive index inducing a change in the scattering properties of the gold structures [32] [Fig. 1 (c)-(e)]. With the widespread use of ITO in displays, photovoltaics, and light-emitting diodes, ITO can be readily manufactured in existing foundries. Although currently there is little existing work on ITO-based metasurfaces, and none to our knowledge using ITO as the scattering material itself, its optical and electrical properties, along with its established use in microfabrication, position ITO as a strong choice for future metasurface designs.

Of all the materials with refractive index less than that of silicon, the earliest reported visible wavelength metasurface lenses utilized silicon nitride (SiN) ($n \sim 2$) nanoposts as scatterers [21]. SiN is also the lowest refractive index material experimentally demonstrated in use for a metasurface [Fig. 1 (g)-(h)] to date and thus provides the widest band gap, with a transparency window extending from the infrared down to the near-ultraviolet regime. This broadband transparency makes SiN a versatile metasurface material, allowing a designer to use the same material and processing techniques for devices at different wavelengths across the transparent region. Furthermore, SiN is a CMOS-compatible material, enabling more streamlined integration with foundry infrastructure already in use for semiconductor microfabrication [33].

There are also other potential transparent metasurface materials, perhaps most notably silicon dioxide. Like SiN, this material not only exhibits a wide band gap but is a material that is widely used and is CMOS-compatible. While lossless, the lower refractive index ($n \sim 1.5$) of this material translates to lower beam deflection efficiency at high angles and reduced focusing efficiency for high NA lenses [34,35]. This reduced performance arises from the decrease in diffraction efficiency that, while minimal at low angles, becomes evident in lower index materials at moderate to high deflection angles [34,35]. While silicon dioxide is preferable compared to a variety of other dielectrics considering its CMOS-compatibility, its manufacturing advantages are matched by those of SiN, but it is inferior in terms of performance. This degraded performance is likely the reason there is an absence of experimentally realized silicon dioxide metasurfaces. For this reason and SiN being the lowest index material experimentally demonstrated in a metasurface, in this paper we primarily detail and summarize state-of-the-art metasurface works based on SiN scatterers.

3. Theory

Metasurface design requires specifying a spatial distribution of scatterers with varying geometric parameters to induce a transfer function for some desired near- or far-field optical response. For traditional diffractive optics relying on gradual phase accumulation, local phase shifts are proportional to the thickness of the element's material, but for metasurfaces the phase shift mechanism operates differently. There are different classes of scattering elements used, but for most dielectric metasurfaces, the phase response arises from either Pancharatnam-Berry phase elements [36,37] and the in-plane anisotropy of the scatterer, or from a cavity-like effect in which the scatterer behaves as a truncated waveguide supporting a mixture of Fabry-Perot resonances. In any case, the distinguishing feature of a metasurface is its subwavelength spatial resolution at the design wavelength, which for normal incidence (or any incidence for lattice spacing less than $\lambda/2$) eliminates higher diffraction orders [38]. This is a powerful feature of metasurfaces compared to multi-level diffractive optics with their super-wavelength spacing, as these elements produce nonzero diffraction orders and correspondingly achieve lower efficiency.

Designing metasurfaces entails selecting a simulation method to compute and test the optical response of the device. The design process can consist of either solving a forward problem, where the structure is designed using some analytical description or intuition to achieve the desired behavior, or an inverse problem in which the desired output is known, and the necessary structure is found via computational optimization. The forward technique has successfully been used to enable a class of flat optics including lenses [4,9,10,39–42],

hologram generators [43,44], polarization elements [45,46], and vortex beam generators [11,46–50]. There are certain classes of devices, however, with non-intuitive phase masks, such as multifunctional elements or multiplexers, which may require inverse design to achieve the desired performance.

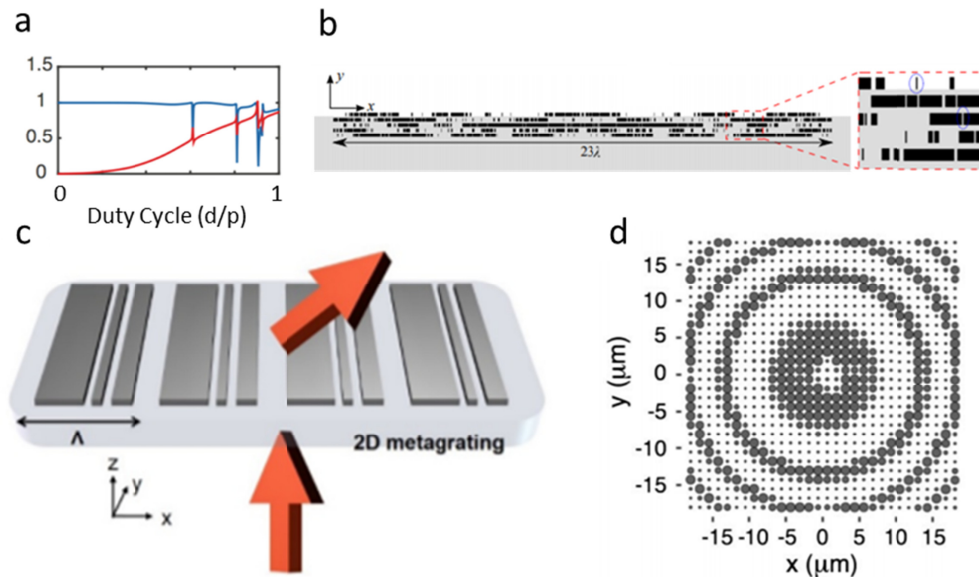


Fig. 2. Metasurface design methodologies. (a) An example transmission amplitude (blue) and phase (red) in units of 2π simulation using rigorous coupled-wave analysis for a forward design of a SiN nanopost metasurface [21]. Adapted with permission from [21]. Copyright (2017) American Chemical Society. (b) An inverse-designed multi-layer metasurface via topology optimization to produce aberration-corrected focusing at four different incidence angles made of silicon (black) and alumina (gray) [53]. (c) Schematic representation of a periodic metasurface beam deflector designed using rigorous coupled-wave analysis and topology optimization [34]. Adapted with permission from [34]. Copyright (2017) American Chemical Society. (d) A sample lens generated via the sphere-based GMMT inverse method for $50\ \mu\text{m}$ focal length at $1550\ \text{nm}$ [54].

3.1 Forward design

Forward design of a metasurface begins with identifying a desired behavior and specifying its transfer function in terms of a continuous phase mask. For many common elements, analytical forms for these masks exist and it is only required to select certain parameters (e.g., focal length, axicon angle, wavelength) based on the desired application. The continuous phase distribution is then converted to a spatially discrete profile, with the period equal to the scatterer lattice spacing. The phase at each position is then mapped to the scatterer design which most closely reproduces the desired phase. The phase response of the scatterers are stored in a library generated by electromagnetic simulations of scatterers using a periodic boundary condition, either by finite-difference time-domain (FDTD) or via rigorous coupled-wave analysis (RCWA) [51] [Fig. 2 (a)]. Once the geometric parameters of the metasurface are known, the whole structure may be simulated via FDTD if computational resources permit. Due to the memory intensive nature of FDTD simulation, often only a portion of the whole metasurface can be simulated. If simulating the whole structure is necessary, a less accurate method based on scalar diffraction theory can be used, treating the metasurface as a complex amplitude mask and evaluating light propagation and performance using a diffraction integral [52].

In the RCWA simulation, the periodic boundary condition ensures all the scatterers in the lattice have identical geometric parameters. When the metasurface is designed, however, the geometric parameters are varied from pixel to pixel, which is inconsistent with the assumptions made for RCWA. If the geometric parameters of neighboring pixels are varied slowly enough, then this discrepancy can be negligible. This assumption is referred to as the unit cell approximation and when it is not valid it can pose significant limitations for the design process. While this approximation holds well for metasurfaces based on high index materials such as metals or silicon [10], optical confinement worsens with decreasing refractive index, as for SiN. This approximation is of less concern when designing devices that are slowly-varying, such as long focal length lenses, but for rapidly varying profiles such as those for holograms, it is necessary to assess the robustness of this approximation. A standard method for doing this is to examine a scatterer's behavior as a function of the lattice constant [10]. As the strength of coupling between adjacent elements is related to the gap between them, if the optical response varies rapidly with spacing, it is an indication that coupling is significant, and that the unit cell approximation is invalid. If, however, the phase and amplitude response of a scatterer remains invariant over a wide range of lattice spacings, then the scatterers are weakly-coupled to one another and it is reasonable to use the scattering response calculated assuming a periodic boundary condition. In this case, the nanoposts can be treated as pixels which behave locally and are unperturbed by their neighbors.

3.2 Inverse design

For the inverse design method, while the desired response is known, the exact metasurface structure to realize that behavior can be challenging to determine by forward methods. To circumvent this, a figure of merit is defined to quantify the performance of the device and upon successive iterations of solving the forward problem and updating the design parameters of the structure, the figure of merit can be optimized until the desired behavior is attained.

There are various existing algorithms for such optimization problems. One promising route is to use topology optimization combined with a finite-difference solver, which has already been applied in the context of designing multi-layer metasurfaces for angular aberration correction of a metalens [Fig. 2(b)] as well as focusing of incident light to the same position over a range of incidence angles [53]. This approach requires definition of a desired phase profile which is included in the figure of merit and the method modifies the spatial permittivity distribution in a binary manner across a set of pre-defined layers. The layer thicknesses in this method are on the order of the wavelength and it inherently accounts for interactions and coupling between the layers. This work used silicon and alumina as the materials of choice but could be extended to lower index material platforms such as SiN as well. Topology optimization has also been used for designing high efficiency single layer beam deflection metasurfaces [Fig. 2(c)] and free-space wavelength splitters, using a wide span of refractive indices (~1.5-3.5), including that of SiN [34]. In this case, RCWA was used to simulate periodic structures and the deflection angle of the unit cell was optimized. Significantly, higher refractive index materials performed better in general, achieving higher efficiencies; however, for low to moderate deflection angles the differences were not as appreciable. For a specified period, the optimized grating structure was similar in shape over a wide range of indices for achieving the same deflection angle, with similar modal structure, yet the difference in efficiency was attributed to greater intra- and inter-mode coupling.

Separately, a work [54] demonstrating inverse design of arrays of dielectric spheres successfully generated single and double layer metalenses using the adjoint method and generalized multi-sphere Mie theory (GMMT). While this work used spheres with a refractive index of 1.52, the index for polymers used in state-of-the-art two-photon polymerization 3-D printers, the algorithm was recently used in a separate study [35] for indices from 1.2 to 3.5, which includes the index for SiN. GMMT is a method based on the T-matrix formalism and can calculate the electromagnetic scattering off an ensemble of spheres [55–57]. Compared to

the FDTD method, which requires extensive computational resources for meshing large structures, the GMMT technique leverages analytical expressions for scattering off spheres to reduce the computational load. As GMMT does not require meshing individual scatterers, the required memory does not scale with system size, but rather the number of spheres and their density and the order to which the field is expanded [57]. By updating the radii of the spheres in the array each iteration, the figure of merit can be optimized by examining the gradient of the figure of merit with respect to the sphere radii using the adjoint method. Leveraging this, successful inverse design and simulation of focusing lenses was shown [Fig. 2(d)], in strong agreement with results computed via FDTD for comparison [54]. The technique was extended to multiple layers of metasurfaces, enabling possible future inverse design of volumetric optical elements with subwavelength sphere-based voxels.

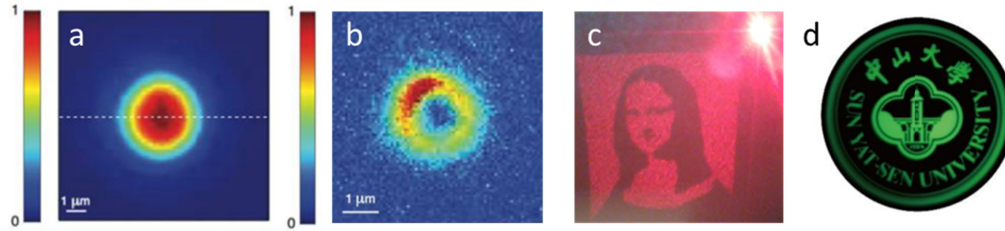


Fig. 3. Outputs from basic SiN metasurface elements. Field profiles captured with a microscope at the focal plane of a metasurface lens (a) and vortex beam generator with $l = 2$ (b) [21]. Adapted with permission from [21]. Copyright (2017) American Chemical Society. (c) Far-field intensity profile of a Mona Lisa pattern generated by a SiN metasurface hologram design. (d) Image captured of a university logo pattern using a SiN metasurface lens [23].

4. Optical elements

4.1 Basic elements

A variety of metasurface-based optical elements using SiN scatterers exist, enabling high efficiency from the visible into the infrared. To design an aspherical lens, the phase obeys the function below

$$\varphi = \frac{2\pi}{\lambda} \left(f - \sqrt{x^2 + y^2 + f^2} \right) \quad (1)$$

where f is the focal length, x and y give the in-plane position, and λ is the operating wavelength. Typically, these lenses comprise arrays of cylindrical nanoposts which are polarization-insensitive. Fabricating the device via a combination of electron-beam lithography and plasma etching, existing SiN based lenses have achieved focusing efficiencies as high as 63% and near diffraction-limited focal spot sizes [21,23,26] [Fig. 3 (a)]. These lenses have been used to perform imaging of patterns in both transmission [23] [Fig. 3 (d)] as well as from scattering light off printed object patterns [26].

In addition to aspherical lenses, SiN vortex beam-generating metalenses have also been realized. The phase for these devices follows the form as below

$$\varphi = \frac{2\pi}{\lambda} \left(f - \sqrt{x^2 + y^2 + f^2} \right) + l\theta \quad (2)$$

where the first term is identical to that of the lens phase, l is the topological charge or integer value of orbital angular momentum, and θ is the azimuthal angle. For $l = 0$, we obtain the phase formula for a lens. These devices generate a helical wavefront and at the focal plane produce a doughnut-shaped beam [Fig. 3(b)], potentially useful for stimulated emission depletion (STED) microscopy applications, where a SiN-based implementation [21] would enable higher efficiency at visible wavelengths.

Hologram-generating metasurfaces using SiN nanoposts also exist. These devices use the Gerchberg-Saxton (GS) algorithm to relate the intensity in the far-field to a phase-mask at the input plane. By mapping the calculated phase to an array of diameters for nanoposts, the desired hologram is achievable in the far-field. Designs were fabricated and illuminated with a 633 nm (HeNe) laser and the output was captured on a camera in the far-field [Fig. 3 (c)].

4.2 Freeform surfaces

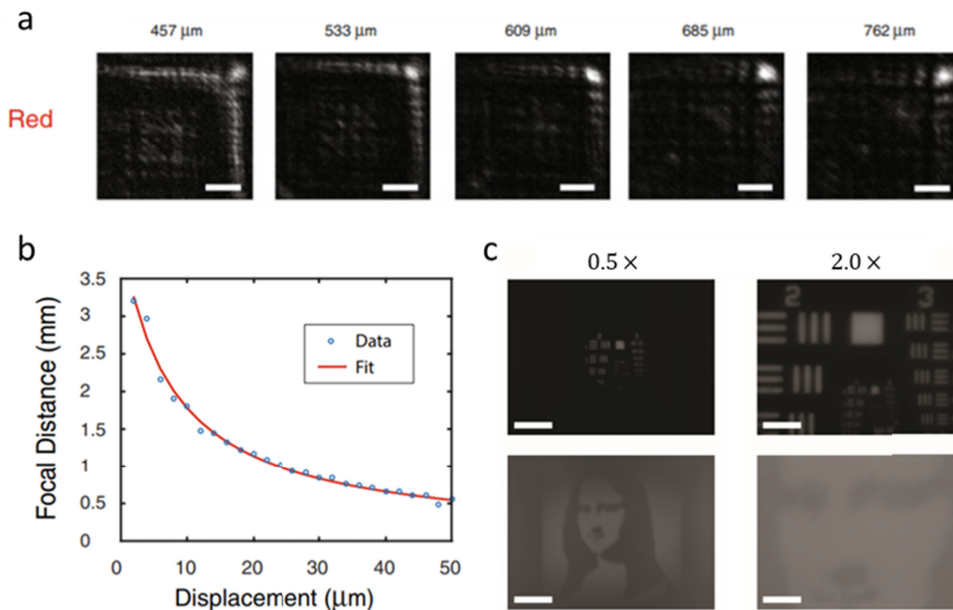


Fig. 4. Freeform SiN metasurfaces. (a) Highly depth-invariant point spread functions measured for a cubic phase metasurface generating an Airy beam at 633 nm wavelength. Scale bar, 18 μm [22]. (b) Measured focal length as a function of displacement for a 150 μm wide metasurface Alvarez lens designed at 633 nm using SiN [22]. (c) Varifocal zoom imaging of both an Air Force test chart and a printed Mona Lisa pattern using a 1 cm wide Alvarez lens at 633 nm using SiN. Scale bar, 1.2 mm [58].

In addition to vortex lenses and holograms, more general SiN-based elements characterized by rotational asymmetry and higher order polynomial surfaces, commonly known as freeform surfaces, have also been reported. Due to the lack of rotational symmetry, it is extremely costly to manufacture freeform refractive optics. While such structures are feasible using multi-level diffractive optics, these are not subwavelength in nature and have correspondingly lower efficiency and furthermore require multiple lithography stages to realize.

With a SiN metasurface platform, cubic polynomial surfaces were fabricated [22] using a single lithography stage. These elements generated Airy beams and the point spread functions of the devices were shown to be invariant over a wide depth range along the optical axis [Fig. 4 (a)]. In addition to single cubic polynomial metasurfaces, Alvarez lenses have been realized using SiN metasurfaces [22], integrating two cubic phase plates of opposite sign. By displacing the two aligned phase plates laterally with respect to one another (i.e., orthogonal to the optical axis), a net quadratic phase function was achieved. By laterally displacing the two plates, a nonlinear change in focal length at 633 nm was provided as the focal length is inversely proportional to the lateral displacement [22] [Fig. 4 (b)], providing a total focal length change of 2.7 mm. In addition to this design, large area 1 cm × 1 cm aperture Alvarez lenses were realized [58] at both 1550 nm and 633 nm using SiN nanoposts. These devices were fabricated using high-throughput stepper photolithography and achieved focal length

ranges of 3.2 cm to 9.8 cm and 9 cm to 30 cm at 1550 nm and 633 nm respectively over the maximum possible lateral actuation range of the structures. These are the largest tunable focal length ranges demonstrated to date for optical metasurfaces. Using the large area visible Alvarez lens, varifocal zoom imaging was performed, keeping the object position fixed and tuning the focal length to shift the image plane, achieving magnifications from $0.5\times$ to $2.0\times$ [Fig. 4 (c)], a $4\times$ zoom range without utilizing any other elements in the imaging path.

5. Optical systems

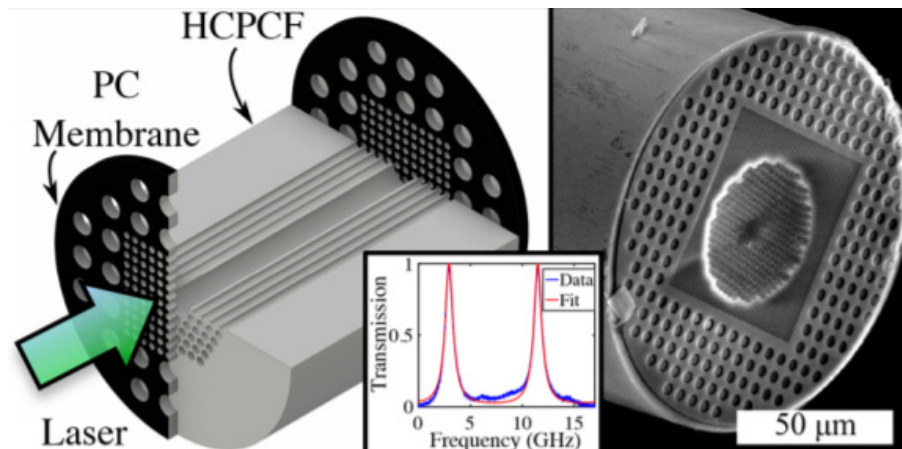


Fig. 5. Hollow core fiber metasurface mirror cavity [25]. Schematic representation (left) and a scanning electron micrograph (right) of the metasurface-based cavity design. The inset shows the measured spectrum and fit. Adapted with permission from [25]. Copyright (2018) American Chemical Society.

The compactness of metasurfaces enables miniaturization of a broad class of optical systems. This allows for implementation in devices where size constraints are stringent, as in machine vision sensors, implantable microscopy, and planar cameras [59]. This has been demonstrated with SiN metasurface systems in optical cavities [25], computational imaging systems [26], and disorder-engineered wavefront shaping [60], providing substantial size reductions while maintaining or enhancing the desired performance. In addition to the size benefits of metasurfaces in general, SiN is particularly well suited for a broad range of applications because of its wide band gap, enabling high efficiency from the near-UV into the infrared. In this section, we expand on some existing optical systems that leverage SiN metasurfaces to enhance performance and reduce size.

5.1 Optical cavities

A metasurface can be used as a high reflectivity mirror without higher diffraction orders. Placing two such mirrors in front of each other, the structures can form a Fabry-Perot cavity. Recently, such a device was realized by transferring two SiN metasurfaces on either end of a hollow core fiber [25] (Fig. 5). The metasurface scatterers relied on holes rather than nanoposts, operating similarly to a photonic crystal lattice. In this manner, the cavity still allowed for gases to diffuse into and out of the cavity. Spectral characterization of the fabricated hollow core fiber metasurface cavity demonstrated Q factors as high as 4.5×10^5 and a finesse of 11. The ability to realize a cavity in this manner has applications in enhanced gas spectroscopy and fiber lasing. Beyond simple metasurface planar mirrors, it may be possible to design metasurface-based diffractive elements to engineer transverse modes, such as flat top beams or arbitrary mode profiles [61] and output beam shapes for fiber-based lasers.

5.2 Computational imaging

Many optical systems today comprise chains of optical components in series to mitigate aberrations and improve image quality. The necessity of having these numerous optics significantly complicates system size, alignment, fabrication, and cost. While metasurface optics has aided the miniaturization of such systems, the computational imaging community has also made significant advancements using simple optical elements in conjunction with software [62,63]. There has been little work, however, towards combining both computational imaging and metasurface optics to realize systems which leverage the advantages of both disciplines.

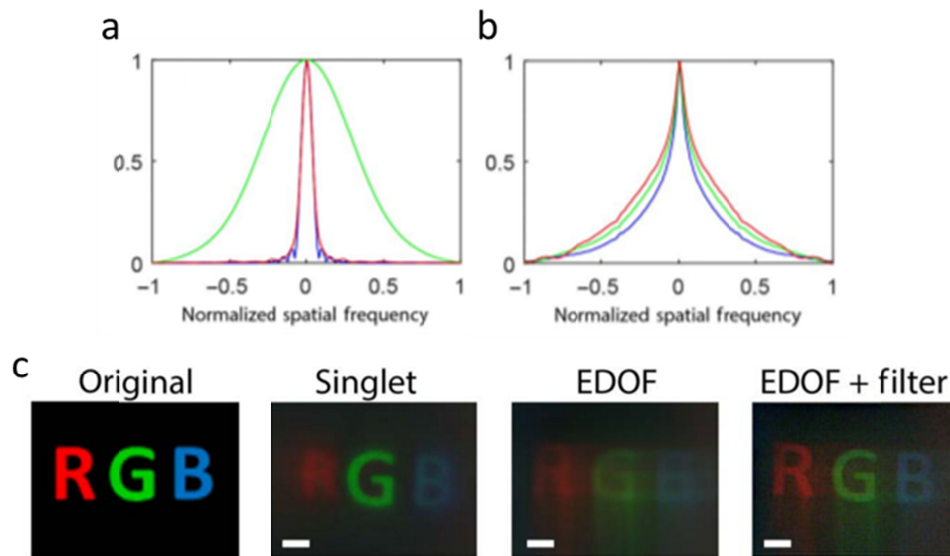


Fig. 6. Metasurface-based computational imaging for full-color imaging [26]. Modulation transfer functions for a singlet metalens (a) and for an extended depth of focus (EDOF) design (b). The colors correspond to the illumination color when measuring the point spread function. (c) Experimentally measured images under white light illumination for a singlet metalens, the EDOF metalens without deconvolution, and the EDOF metalens image after deconvolution. Scale bar, 20 μm .

Recently, a system design consisting of an extended depth of focus metalens combined with a post-capture software filter enabled full-color imaging across the visible regime using white light [26]. Imaging with white light had been a longstanding challenge in the metasurface community as metasurfaces exhibit severe chromatic focal shifts. By designing a SiN metalens with a phase mask that provided an extended depth of focus, upon shifting of the focal plane due to longitudinal chromatic aberration, light would still impinge on the sensor plane. As such, a spectrally invariant point spread function (PSF) was achieved and enabled deconvolution with a single digital filter, allowing for a fast calibration procedure by measuring a single PSF [64,65]. This spectrally invariant point spread function provided modulation transfer functions (MTFs) that were invariant under wavelength change and without zeros in their spatial frequency spectra, unlike those of a singlet lens, which are highly chromatic and result in an unrecoverable loss of information because of the presence of zeros in their spectra [Fig. 6(a)-(b)]. Object patterns imaged with white light were deconvolved based off the calibration measurement, generating in-focus images, whereas those captured with a traditional metalens without any post-processing exhibited substantial chromatic aberrations [Fig. 6 (c)]. Currently, the final filtered images still exhibit substantial noise and asymmetric artifacts because of the shape of the PSF. Overcoming these challenges

will require more sophisticated calibration protocols, deconvolution algorithms, and optimization of the metasurface phase mask.

5.3 Disorder-engineered metasurfaces for wavefront shaping

Disordered media often complicate the task of transforming a wavefront. Prominent examples include imaging through biological tissue or other highly scattering media such as fog, which distort incident wavefronts and hinder image formation. Some disordered media, however, can be used to enhance wavefront shaping capability, leveraging multiple scattering to expand both the spatial extent and range of wavevectors in an optical system [66–72]. In this case, the employed disordered medium must be fully characterized to understand its effect on an incident wavefront. In knowing the effect of the disordered medium, the distortion it introduces can be removed via post-processing or exploited in conjunction with a source to achieve more sophisticated functionalities [70–73].

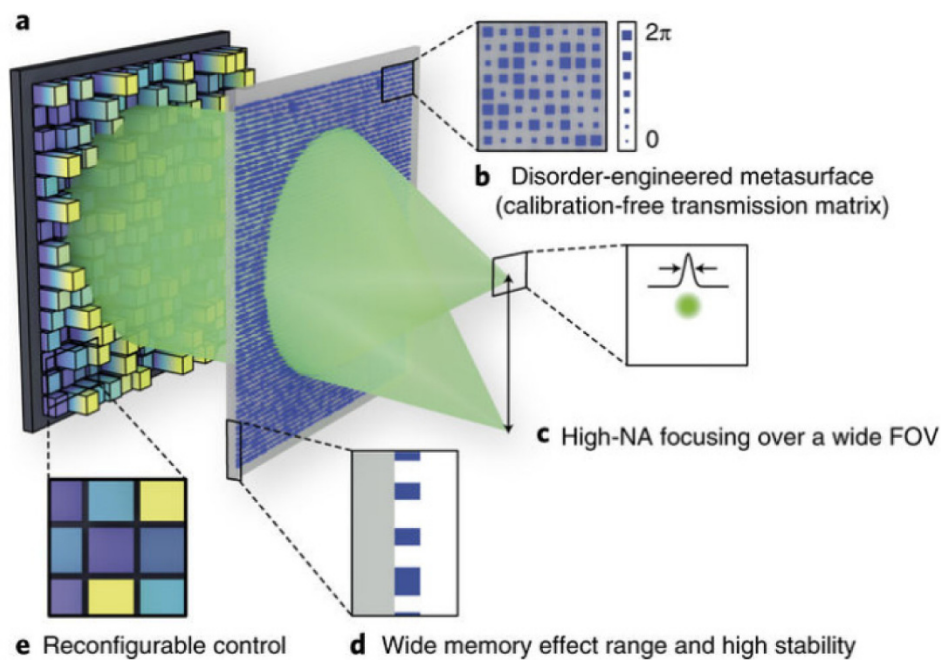


Fig. 7. Disorder-engineered SiN metasurface system used for wavefront shaping [60]. The designed system comprised a spatial light modulator (a) with reconfigurable pixels (e) and a disorder-engineered metasurface made of square nanoposts of SiN on a quartz substrate (b). By accessing a broader real and wavevector space, the system enabled high-NA focusing over a wide FOV (c). The thinness of the element provided a wide memory effect range and its static nature after fabrication made for a highly stable disordered medium.

Calibration of the medium typically consists of measuring its transmission matrix, necessitating a sequence of $O(N)$ measurements to map N input-output connections [72,74–77]. For many applications, N more than 10^{12} is necessary to achieve an accurate mapping, requiring a very large number of measurements, which can be prohibitively time consuming. Recently, however, this cumbersome calibration procedure was circumvented by engineering a disordered medium using a silicon nitride metasurface [60] [Fig. 7 (a)-(b)]. The metasurface was designed to isotropically scatter incident light in the far-field, using the Gerchberg-Saxton algorithm to generate a hologram with uniform amplitude and random phase. As the phase mask of the metasurface was known a priori, its effect on incident light was known without requiring measurement of its transmission matrix. Instead, a quick two step alignment procedure was used to position the metasurface in the optical path. In conjunction with a

reconfigurable spatial light modulator [Fig. 7(e)], the system demonstrated high-NA focusing over a wide field of view [Fig. 7(c)]. The selection of SiN as the metasurface material enabled higher efficiency performance at visible wavelengths, suitable for biological fluorescent imaging applications. The system was used to image *Giardia lamblia* cysts with fluorescent labels, demonstrating the resolution of a 20x objective with the field of view of a 5x objective. The thinness of the element relative to conventional disordered media enabled a high degree of correlation under angular tilt, which is known as the optical memory effect [Fig. 7(d)]. Additionally, as the metasurface is unchanging after fabrication, it is extraordinarily stable, whereas many disordered media are dynamic and transmission matrices often become decorrelated with time.

6. Future directions

While there have been many substantial research advancements in SiN and other metasurfaces with refractive index less than that of silicon, there is still a wide array of challenges and research directions to be explored. In terms of design methodology, there is significant room for improvement and adaptation of inverse design algorithms for use in making more advanced devices. Currently, these inverse design techniques have only been applied to relatively simple metasurface structures, such as beam deflectors and lenses [34,53,54]. The real benefits of inverse design, however, will only come when it can deliver devices with non-intuitive designs, such as multiplexers and multifunctional elements, that are beyond what can already be done using traditional forward-based methods. Much of this work will entail defining performance metrics and figure of merit design. Aside from inverse design of metasurfaces alone, co-optimizing both the optics and post-processing software as a full pipeline [63] is a possible route to improve system performance for computational imaging with metasurfaces. This approach exists in the context of refractive and multi-level diffractive optics but has yet to be applied to metasurfaces directly, where the inherent subwavelength resolution can potentially deliver further benefits. Furthermore, computational imaging with metasurfaces has only focused on mitigating chromatic aberrations [26], whereas there is no existing work specifically targeting geometric aberrations. Tackling chromatic and geometric aberrations simultaneously will be a challenging but worthwhile research direction.

Beyond design method considerations, there are also material and scalable manufacturing challenges to be examined. Using even lower index materials, such as organic polymers, may provide additional benefits, including the possible use of printable photonics or two-photon polymerization-based 3D printing for fabricating devices. Specifically, roll-to-roll printing could significantly reduce the manufacturing cost of metasurfaces, which could potentially be used for making cheap concentrators for photovoltaics. These printing techniques could be extended to making volume optics comprising several sets of metasurfaces working in tandem to enable more advanced multifunctional or multiplexing capabilities [78]. Transitioning to even lower index materials, however, will entail having to overcome the drop in beam deflection efficiency associated with decreasing refractive index [34]. Appropriate material selection could also facilitate realization of arbitrarily reconfigurable visible wavelength metasurfaces, by using ITO or other transparent conducting oxides, or complex oxides exhibiting large electro-optic coefficients [79]. Arbitrary subwavelength tuning of two-dimensional metasurfaces, however, is a significant electronics control problem on its own, with the use of even lower index materials being an additional constraint for improving efficiency at visible frequencies.

7. Conclusion

Metasurfaces with a refractive index less than that of silicon have generated substantial attention in the optics community in recent years. As the refractive index of a dielectric obeys the empirical Moss relation, the band gap increases for lower indices. This relationship

motivated a push away from metallic and silicon-based resonators to lower index materials, which provide transparent operation at visible frequencies. In this review, we primarily examined SiN as it is the lowest refractive index material experimentally demonstrated as a metasurface scatterer to date. Additionally, the CMOS compatibility of this material makes it particularly attractive for large-scale manufacturing. We conducted a comprehensive overview of the forward and inverse design processes employed for metasurfaces and then discussed state-of-the-art optical elements and systems that leverage SiN structures. As optical elements, SiN nanoposts have enabled visible frequency metasurface lenses, holograms, and freeform surfaces. When integrated with other components, SiN metasurfaces have found use in a diverse array of applications ranging from disorder-engineered wavefront shaping and computational imaging, to hollow core fiber-based optical microcavities. With their compact form factor, CMOS compatibility, and unprecedented capabilities for efficiently modifying wavefronts with subwavelength resolution, the future of SiN metasurfaces looks promising.

Funding

Amazon Catalyst; Samsung-GRO; Intel Early Career Faculty Award; University of Washington start up fund.

Acknowledgments

This work was facilitated through the use of advanced computational, storage, and networking infrastructure provided by the Hyak supercomputer system at the University of Washington (UW). Part of this work was conducted at the Washington Nanofabrication Facility / Molecular Analysis Facility, a National Nanotechnology Coordinated Infrastructure (NNCI) site at the University of Washington, which is supported in part by funds from the Molecular Engineering & Sciences Institute, the Clean Energy Institute, the Washington Research Foundation, the M. J. Murdock Charitable Trust, the National Science Foundation and the National Institutes of Health.